Performance Evaluation of Phase and Weather-Based Models in Atmospheric Correction With Sentinel-1Data: Corvara Landslide in the Alps

Mehdi Darvishi, Giovanni Cuozzo, *Member, IEEE*, Lorenzo Bruzzone, *Fellow, IEEE*, and Faramarz Nilfouroushan

***Abstract*—Phase delay caused by atmospheric effects due to spatial and temporal variations of pressure, temperature, and water vapor content is one of the major error sources in estimation of ground deformation by interferometric synthetic aperture radar (InSAR>). Therefore, accuracy of ground deformation measurement is highly contingent on the robustness of the atmospheric correction techniques. These techniques rely either on auxiliary data such as numerical weather models (NWMs) or on the analysis of the interferometric phase itself. The accuracy in phase delays estimation of mixing effects of turbulent delay in atmosphere and stratified delay in lower troposphere is a key factor in determination of performance of each technique. Hence, the performance evaluation of the techniques is required in order to assess their potentials, robustness, and limitations. This article analyzes and evaluates the performance of four NWMs (i.e., ERA-Interim, ERA5, MERRA2, and WRF) and two phase-based techniques (i.e., linear and power law) to estimate phase delay using Sentinel-1A/B data over the Corvara landslide located in the Alps. The GPS data and GACOS product were used to validate the results. We generally found that ERA5 outperformed among other weather models with a phase standard deviation reduction of 77.7% (with respect to the InSAR phase), a correlation coefficient of 0.86 (between InSAR phase and estimated tropospheric delay) and a less significant error in the velocity estimation of the landslide.**

***Index Terms*—Atmospheric correction, GPS, InSAR, phase and weather-based models, phase delay, Sentinel-1.**

I. Introduction

SYNTHETIC aperture radar interferometry (InSAR) is a powerful geodetic tool for detection and quantification of earth surface deformation. However, it suffers of possible artifacts due to atmospheric phase delay. Atmospheric delays are predominately composed of ionospheric and tropospheric components. Ionosphere [i.e., total electron content (TEC)] can cause a phase advance on microwave signals. Thus, it has a severe effect on L-band than C- and X-band, with a magnitude inversely proportional to the signal frequency [1]. Tropospheric variation in time and space of water vapor, pressure, and temperature causes a phase delay [2]. Changes in relative humidity of 20% lead to more than 290 m of topographic error for a 100 m baseline measurements (independently of wavelength), and relative humidity in the lower part of the troposphere (<5 km) could potentially induce up to few centimeters interferometric phase delay [2]–[4].

This phase delay could reach approximately several centimeters and often affects the deformation signal [5]. This additional contribution in interferogram (IFG) results from a turbulent component affected by troposphere dynamics (also called wet delay) and stratification or a long-wavelength component induced by the lower atmosphere parameters such as pressure, temperature, and relative humidity (also called dry delay) [5], [6]. Many studies have been developed to mitigate the negative effects of the turbulent component as random component in space and time in IFGs by applying the temporal and spatial filtering [7]–[9] to time series of SAR data.

Stratified tropospheric delay can cause a long-term bias in estimates of the deformation signal, where stacking-based methods are used, especially when seasonal variations have not properly been sampled in time [10]. Different methods have been proposed to correct the tropospheric phase delay in SAR data which can be generally split into two groups: First, phase-based methods (or empirical methods), relying on the correlation between interferometric phase and topography in either a nondeforming area [11], [12] or a deforming area (power law) [13], second, weather-based models (or predictive methods) relying on weather parameters (e.g., pressure, temperature, and relative humidity) of numerical weather models (NWM) [4]–[14], [15] such as ERA-Interim [14] and ERA5 provided by ECMWF (European Center for Medium-Range Weather Forecasts), Generic Atmospheric Correction Online Service for InSAR (GACOS) (based on HRES-ECMWF)[16], global forecast system (GFS) data using weather research and forecast (WRF) model [17], [18], modern-era retrospective analysis for research and applications (MERRA-2). Satellite spectrometers, utilizing

Manuscript received December 19, 2018; revised September 27, 2019 and November 25, 2019; accepted December 16, 2019. Date of publication March 20, 2020; date of current version April 20, 2020. *(Corresponding author: Mehdi Darvishi.)*

Mehdi Darvishi is with the Institute for Earth Observation, Eurac Research 39100 Bolzano, Italy, and also with the Department of Information Engineering and Computer Science, University of Trento, 38122 Trento, Italy (e-mail: mehdi.darvishi@unitn.it).

Giovanni Cuozzo is with the Institute for Earth Observation, Eurac Research 39100 Bolzano, Italy (e-mail: giovanni.cuozzo@eurac.edu).

Lorenzo Bruzzone is with the Department of Information Engineering and Computer Science, University of Trento, Trento, Italy (e-mail: lorenzo.bruzzone@unitn.it).

Faramarz Nilfouroushan is with the Faculty of Engineering and Sustainable Development (ATM), University of Gävle, 801 76 Gävle, Sweden, and also with the Geodata Division, Lantmäteriet, 802 64 Gävle, Sweden (e-mail: faramarz.nilfouroushan@hig.se).

Digital Object Identifier 10.1109/JSTARS.2020.2969726

observations of atmospheric water vapor, could also be used to estimate wet delay such as Moderate Resolution Imaging Spectroradiometer (MODIS) [19] and Medium-Resolution Imaging Spectrometer on board Envisat (MERIS) [20]. In addition to that, point-wise GPS measurements can be used to estimate zenith total delay (ZTD), zenith wet delay (ZWD, and zenith hydrostatic delay (ZHD [21]–[23] alone or in combination with spectrometer data [24].

Each method has its own drawbacks and advantages. For instance, linear methods have two main limitations: First, need for a nondeforming area (this could be overcome by applying a spatial-band filtering sensitive to deformation [25] or using a deformation model [26]), second, the simple hypothesis of dependency between phase and elevation does not take into account the spatial variation of atmospheric characteristics. The power law technique [13] was proposed to either operate on a deforming region or consider the spatial variation between phase and elevation.

In this study, we use phase-based models, including linear and nonlinear (power law) models, numerical weather model (NWM) models involving ERA-Interim, ERA5, MERRA2, and WRF, multispectral data (MODIS) and GPS data to estimate phase delay on Sentinel-1A/B data and evaluate the performance of them. Three steps are carried out as follows.

1) Cross comparison among the ZTD, ZWD, and TWD derived by GPS with its counterparts obtained by NWM-based models.
2) Cross comparison between the InSAR tropospheric phase delays estimated by phase and NWM-based models in a regional scale.
3) Cross comparison between the GPS stations velocity and the velocity corrected by the phase and NWM-based models in a local scale (i.e., the active Corvara landslide in Italy).

In addition to the GPS data, we used the GACOS product as reference to cross validate the results in all steps.

The efficiency of the atmospheric correction methods is restricted by the different factors. For example, Generally, NWM models have a low-spatial and temporal resolution and might not be available at the time of SAR data acquisition. Therefore, interpolating in time and resampling in space could potentially lead to an unwanted uncertainty [17]. GPS data are known as accuracy pointwise measurements but are not available everywhere. Multispectral data can only be used in the cloud-free and daylight conditions.

II. Approach

A. Atmospheric Correction Methods

Phase delay of radar signal induced by the atmosphere can be defined by the atmospheric refractivity *N*

$$N = \underbrace{k_1 \frac{P}{T}}_{\text{Hydro}} + \underbrace{\left(k_2 \frac{e}{T} + k_3 \frac{e}{T^2}\right)}_{\text{Wet}} - \underbrace{\left(4.03 \times 10^7 \frac{n_e}{f^2}\right)}_{\text{Iono}} + \underbrace{1.4W}_{\text{Liquid}} \tag{1}$$

where T is the temperature (Kelvin), P is the pressure (hPa), e is the partial pressure of water vapor (hPa), n_e is electron number density per cubic meter, f is radar frequency, and W is the liquid water content (g/m^3), while $K_1 = 77.6$, $K_2 = 23.2$, and $K_3 = 3.75 \times 10^5$ are empirical coefficients [27]. The refractivity term is composed of four components: hydrostatic or dry (N_{hydro}), wet (N_{wet}), ionospheric (N_{iono}), and liquid (N_{liquid}). Each component can partially cause some phase delay (i.e., $N_{\text{hydro}} + N_{\text{wet}}$) or phase advance ($N_{\text{iono}}$) of radar signal. The effect of N_{iono} is often significant for longer wavelengths (e.g., P- and L-band), whereas for sensors with shorter wavelengths (e.g., X- and C-band) is negligible. The liquid component affects the refractivity just in case of saturated atmosphere and for the InSAR application can be ignored [5]. Therefore, one-way tropospheric delay (S_{trop}) and two-ways tropospheric phase delay ($\emptyset_{\text{trop}}$) can be characterized by integrating over the refractivity along radar line-of-sight at a given height (h) as follows:

$$S_{\text{trop}} = \frac{10^{-6}}{\cos\theta} \int_0^h \left(N_{\text{hydro}} + N_{\text{wet}}\right) dh \tag{2}$$

$$\phi_{\text{trop}} = \frac{-4\pi}{\lambda} S_{\text{trop}} \tag{3}$$

where θ indicates the incidence angle, $-4\pi/\lambda$ is a factor to convert from pseudorange increase to phase delay and λ the radar wavelength [5].

B. Phase-Based Tropospheric Delay Estimation (Linear)

Tropospheric phase delay based on the linear model assumes that a linear relation between the interferometric tropospheric delay and the topography exists. This phase delay is estimated from data in a nondeforming region

$$\Delta\phi_{\text{trop\_linear}} = k_{\Delta\phi} h + \Delta\phi_0 \tag{4}$$

where the coefficient $k_{\Delta\varnothing}$ indicates a constant relating the interferometric tropospheric phase to topography, h the altitude, and $\Delta\emptyset_0$ is related to a constant shift applied to the whole IFG that can be therefore neglected [13].

C. Phase-Based Tropospheric Delay Estimation (Nonlinear)

Tropospheric phase decreases by decreasing the height and relative delays among different acquisitions are only significant up to a certain altitude h_0 (where phase delays converged to zero), the relationship between phase and topography can be empirically approximated by the following power law function [13]

$$\phi_{\text{trop}} = k_\phi (h_0 - h)^\alpha + \Delta\phi_0 \; h < h_0 \tag{5}$$

where $k_\varnothing$ is an unknown coefficient relating to phase and topography, which varies spatially in each acquisition. The parameters α and $\Delta\varnothing_o$ are the power law decay component and the phase delay at the reference height, respectively. The interferometric phase delay (i.e., difference between phase delay of master and slaves acquisitions $\Delta\phi_{\text{trop}} = \phi^m_{\text{trop}} - \phi^s_{\text{trop}}$) is obtained according to the following

$$\Delta\phi_{\text{trop}} = (k_{\phi m} - k_{\phi s})(h_0 - h)^{\alpha}, k_{\Delta\phi} = (k_{\phi m} - k_{\phi s}) \tag{6}$$

where $k_{\Delta_\varnothing}$ can be estimated by applying band-filtered phase and topography to (6) due to the fact that the tropospheric phase is present in all wavelength scales and the spatial frequency band is relatively not sensitive to other signals such as incorrect orbit and ionospheric delay [13]–[25].

D. NWM-Based Tropospheric Delay Estimation

The second type of the correction method exploits the availability of external datasets. NWM has a great potential in phase delay estimation (PDE) in InSAR applications as an external data. In this approach, atmospheric variables are used to estimate the refractivity components (1). These NWM models are various in terms of spatio-temporal resolution and data provider. Therefore, the use of each model to estimate spatiotemporal variations of both water vapor and temperature (wet delay) and pressure (hydrostatic or dry delay) might lead to a different accuracy and precision in PDE. To determine the robustness and weakness of each NWM model, we use ERA-Interim, ERA5, MERRA2, and WRF models for PDE and GACOS and GPS data for purpose of the results accuracy assessment.

E. Multispectral Data

The MODIS data can be used to estimate the wet component of refractivity under cloud-free and daylight conditions. Five near-infrared (IR) MODIS channels comprising three water vapor absorption and two no absorption are usually used to estimate water vapor. MODIS could retrieve water vapor using observations of water vapor attenuation of reflected solar radiation in the near-IR channels up to an accuracy of 5%–10% [24]–[28]. Comparison of water vapor estimated by MODIS data to GPS and radiosonde pointed out that MODIS overestimates water vapor by a scale factor of 1.07–1.2. Therefore, MODIS-driven wet delay should be calibrated before using in InSAR atmospheric correction [29].

III. Case Study and Dataset

The case study is an active landslide (i.e., Corvara) located in the Autonomous Province of Bolzano-South Tyrol, in the Italian Alps. It is characterized as a complex earth slide-earth flow with annual displacement rates of up to 20 m [30]. This landslide frequently causes damages to the national road SS 244, the ski infrastructures, and the nearby golf course. The Corvara landslide has been monitored for several decades by different systems [31]–[33]. Eighteen Sentinel-1A/B images in descending orbit and interferometric wide swath mode covering from July 22 to November 1 in 2017 at the same acquisition time (5:18 A.M. UTC) were collected over the Corvara landslide. The selection of the descending orbit was because the motion direction of the most important part of the landslide (i.e., the left part, which is next to both the urban infrastructure and the national road that are highly prone to be affected by the landslide movement) is aligned to the Line of Sight (LOS) of the descending mode. As we were in the field for the monthly GPS measurements, we are completely sure that the selected data do not content any snow at the landslide location and the absence of the snow in the case study area was double checked on Sentinel-2 data. Although the Corvara landslide is surrounded by the mountains, the geographical location of these mountains (mainly covered by snow or glaciers) is much far from the Corvara landslide (at least 5 km). Thus, snow melting of the remote mountains cannot affect or trigger the landslide. The GPS monitoring system in Corvara shows that the main cause of the landslide movement is related to the local factors mainly due to the special geological structure of the region right beneath the landslide. Due to the course resolution of weather data and in order to have a better understanding of the tropospheric turbulent and stratified changes, a larger extent of the study area was selected (i.e., 15×15 km) than the portion of the landslide area only (i.e., 3×1.5 km). Fig. 1 shows the extent of Sentinel-1 data used for tropospheric correction purpose and the boundary of the Corvara landslide. We used four permanent GPS stations as references for both the tropospheric delay estimation and the results validation. The stations no. 8, 54, and 58 located within the landslide boundary were used to estimate the landslide velocity, while CIAM GPS station was utilized to estimate zenith total delay (ZTD), ZWD, and ZHD components of the troposphere in a two-hours of time span (herein between 4 and 6 A.M.) [Fig. 1(a), (b), and (d)]. The characteristics of the weather data used in the tropospheric correction are presented in Table I. NWM models involving Era-Interim and ERA5, GFS data (http://rda.ucar.edu/datasets/ds335.0/) and MERRA-2 data (https://gmao.gsfc.nasa.gov/reanalysis/MERRA-2/) were utilized to compute phase delay through pressure, temperature, and relative humidity parameters extracted from the NWM models using (1). The ZDT was derived from the GACOS service (http://ceg-research.ncl.ac.uk/v2/gacos/), which relies on the HRES data [16].

The total perceptible water vapor parameter derived from MODIS data was used to estimate the wet component of tropospheric delay. A GPS permanent station (CIAM) of South Tyrolean POsitioning Service (STPOS) managed by Bolzano/Bozen Province was utilized to retrieve the tropospheric parameters. Table I summarizes the specifications of the data used in this study.

Sounding data providing height profile of atmospheric characteristics such as temperature, pressure, and relative humidity were used to estimate refractivity with the power law method. These data were derived from the Rivolto station provided by the Department of Atmospheric Science of the University of Wyoming (http://weather.uwyo.edu/upperair/sounding.html).

IV. Data Processing and Methodology

A. SAR Data Processing

The Sentinel-1A/B IFGs were generated by using the software SNAP v6 (ESA Sentinel Application Platform v6), the Permanent Scatterers Processing (PS) was performed by StaMPS v3.3 (Stanford Method for Persistent Scatterers) [34] and the phase and NWM-model tropospheric corrections were carried out by TRAIN v3 (Toolbox for Reducing Atmospheric InSAR Noise) [17].

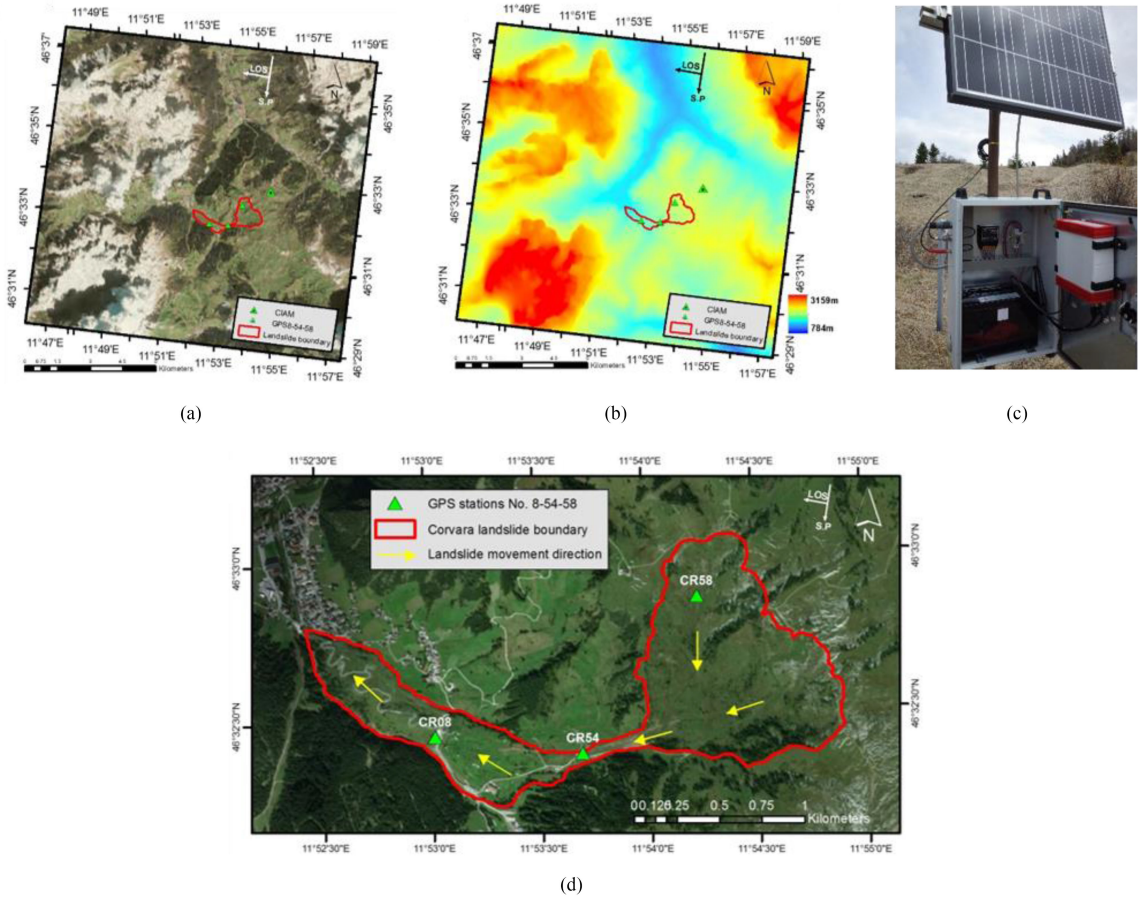

Fig. 1. Study area and GPS stations. (a) Extent of the Sentine1-A/B image used for data processing. (b) The imaged Digital Elevation Model (DEM) from SRTM (30 m) data for the study area. In both (a) and (b), the extent of the Corvara landslide (with the red boundary), three permenant GPS stations (No. 8, 54, and 58 within the red boundary) and one permanent GPS station belonging to the Bolzano Province (the CIAM located out of the landslide border) are indicated. (c) A photograph showing the CR58 equipments including the battery, GPS receiver, and solar panel. The recorded data of each permanent GPS station are transmitted by the mobile network to the servers of the Eurac Institute for Earth Observation. (d) A magnified view of the Corvara landslide with its main motion directions.

TABLE I
CHARACTERISTICS OF GPS, NWM MODELS, SOUNDING, AND MODIS DATA

Data/models	Type	Temporal Res.	Spatial Res.	P. lev.	H-delay	W-delay	H+W	Latency
ERA-Interim	weather	6-hourly	79km	37	Yes	Yes	Yes	several months
ERA-5	weather	Hourly	31km	37	Yes	Yes	Yes	near real-time
GACOS (HRES)	weather	6-hourly	9-12km	137	-	-	Yes	near real-time
GFS	weather	3-hourly	5km	37	Yes	Yes	Yes	near real-time
MERRA-2	weather	3-hourly	50km	42	Yes	Yes	Yes	5 months lag
MODIS	spectrometer	daily	1km	-	-	Yes	Yes	60 - 125 minutes
Sounding data	weather	6-hourly	1 station	115	Yes	Yes	Yes	near real time
GPS	pointwise	30 second	4 stations	-	Yes	Yes	Yes	real-time

H and W indicate the hydrostatic and wet components, respectively, while Res. and P. lev. indicate the resolution and pressure level, respectively.

In the PS processing, five main steps were performed as follows:

1) Initial PS pixel selection by setting 0.4 and 3×2 values for the amplitude dispersion index and the range/azimuth patch sizes, respectively.
2) Estimation of phase noise value for each PS candidate obtained using filtering with a window size of 32×32 pixels (a tradeoff between the S1 pixel size (15×15 m) and the extent of the S1 image) with spatial wavelength of 800 m) using the iterative approach.
3) PS pixel selection based on its noise characteristics.
4) Refinement of the previously selected pixels using a standard deviation threshold of 1.
5) Correction of spatially-uncorrelated look angle error [34].

The weather-based models such as ERA-Interim and ERA5 were directly downloaded and the aforementioned parameters were extracted. The GFS data first processed by WRF model using WRFv3 and WPS packages and the parameters of the domain and parent grid ratio were set 2 and 1/5, respectively, leading to nesting a spatial resolution of 5 km [35]. Four weather

parameters consist of temperature (K), pressure levels (Pa), relative humidity (in %), and geopotential (m) were extracted from all weather-based models to estimate refractivity. As the hydrostatic components could be calculated up to 25–30 km height to compare the NWM model results with GPS-derived atmospheric parameters, we set 30 km as reference height to estimated refractivity in (1). In the case of MODIS data, water vapor IR band from MOD05_L2 product was used to estimate the wet component of the refractivity. Since the water vapor information in cloudy conditions is not valid, the water vapor IR bands were masked with the cloud-cover band provided by MODIS data with a probability of 95%. We then applied the threshold of 80% minimum free-cloud coverage to the water vapor IR band. It turned out that most of MODIS data were rejected under the defined threshold due to the frequent cloud coverage over the study area. This situation did not allow us to go further and estimate interferometric phase delay. Nevertheless, we will present the interferometric phase delay obtained from the nonfree cloud MODIS data in the result section.

The same four weather variables were extracted from the sounding data to approximate the parameters of the power law in (5). In power law processing, the scaled topography and phase were filtered in different bands using 1-D and 2-D Fourier band filtering involving 9 bands from 500 m to 10 km [13]. As the landslide area is small, we set only one patch to estimate the spatial variable of the power law.

B. GPS Data Processing

The CIAM GPS-station data provided by South Tyrolean Positioning Service (STPOS) and corresponding to the Sentinel-1 acquisition days was processed. We processed the data by GAMIT-GLOBK v10.61 software [36] and used the VMF1 mapping function to estimate tropospheric delay parameters for the time span of 4–6 A.M. corresponding to Sentinel-1 data acquisition time (i.e., 5:18 A.M.). The VMF1 NWM as computed by TU Vienna [37] provides 6-h intervals surface pressure data gridded by MIT in yearly grid files for GAMIT users. The VMF1 mapping function is used to compute the "dry" part of the troposphere ZHD. The ZWD due to water vapor and the local gradient parameters were estimated for CIAM station and for every 2 h using GAMIT software. The methodology used in this study is presented in Fig. 2.

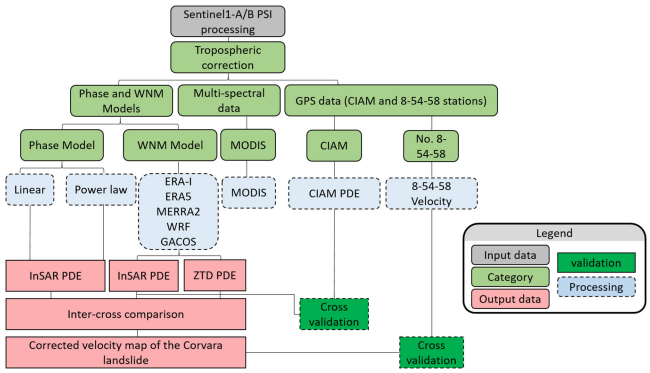

Fig. 2. Flowchart of the methodology used in the study. PDE refers to phase delay estimation.

V. Results

A. GPS Versus Weather-Based Model (Zenith Delay)

In order to evaluate the performance (i.e., accuracy and precision) of NWM models in tropospheric PDE estimation, ZDT, ZHD, and ZWD derived by CIAM GPS station were cross correlated with the same parameters estimated by five NWM models plus GACOS result. As the GACOS provides only ZTD (ZH+ZW) product, hence, only GACOS-ZTD has been compared with ZTD of GPS. Three statistical parameters are composed of root mean square error (rmse), correlation coefficient (R), and standard deviation (std) were used for performance assessment based on the following simple linear models (see Fig. 3)

$$\mathrm{GPS}_{Z(\mathrm{THW})D} = \mathrm{Slope} \times \mathrm{Weather\ Models}_{Z(\mathrm{THW})D} + \mathrm{Intercept}. \quad (7)$$

In terms of std and rmse parameters of ZTD, ERA5 with the std of 2.8 cm and GACOS with the rmse of 0.8 cm presented the most precise and accurate results among other NWM models. In terms of std and rmse of ZWD and ZHD parameters, ERA5 generally provided the most precise and accurate results. In all cases, ERA5 presented the highest correlation among other its counterparts.

B. GPS Versus NWM Models (InSAR Delay)

To estimate InSAR tropospheric delay, we first projected ZTD on the slant range of SAR geometry by applying the factor of $1/\mathrm{Cos}\theta$, and then applying the factor of $-4\pi/\lambda$ to convert from pseudorange increase to phase delay (Hanssen), where θ and λ indicate the incident angle and wavelength, respectively. To achieve the interferometric tropospheric delay the subtraction of tropospheric delay between master and slave acquisition times was used (i.e., $\Delta\emptyset_{\mathrm{trop}} = \Delta\emptyset_{trop}^{slv} - \Delta\emptyset_{trop}^{mst}$). This procedure was employed on ZTD derived from the GPS data corresponding to the master and slave dates (see Fig. 4).

The map of InSAR tropospheric corrections for 18 IFGs using five NWM models and MODIS data are presented in Fig. 5.

The estimated InSAR tropospheric correction maps for all NWM models generally present a relative qualitative agreement respect to each other and show a high correlation with the elevation in most of the IFGs. As the wet component obtained by MODIS was under nonfree cloud conditions, the related result is not reliable to consider it in the rest of our study.

C. Phase-Based Model (Linear)

The linear relation between the unwrapped phase and height is plotted in Fig. 6. The DEM-correlated errors (i.e., correlation between perpendicular baseline and unwrapped phase) were already subtracted from the unwrapped phase. The tropospheric linear delay map estimated using (4) is presented in Fig. 7.

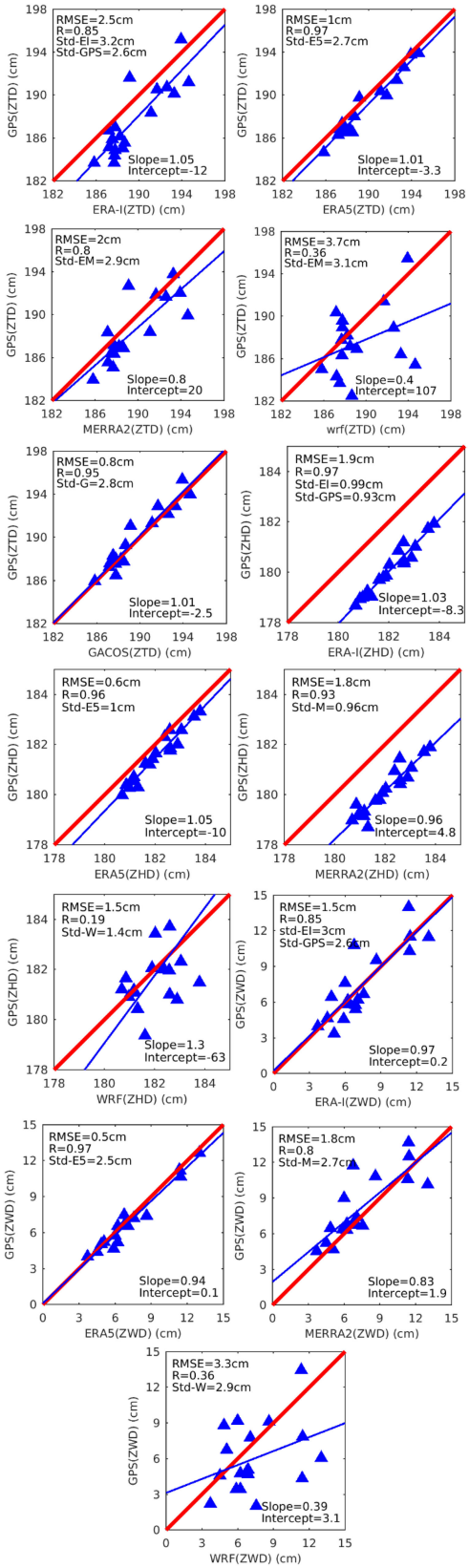

Fig. 3. The ZTD, ZHD, and ZWD parameters of CIAM station versus ZDT, ZHD, and ZWD parameters (the blue triangles) derived by five NWM models contain ERA-Interim (EI), ERA5 (E5), MERRA2 (M), WRF (W), and GACOS (G) (only ZDT). The slope and intercept values (the blue line) of the linear equation and statistical parameters have been estimated for each model. The red line shows the 1:1 line.

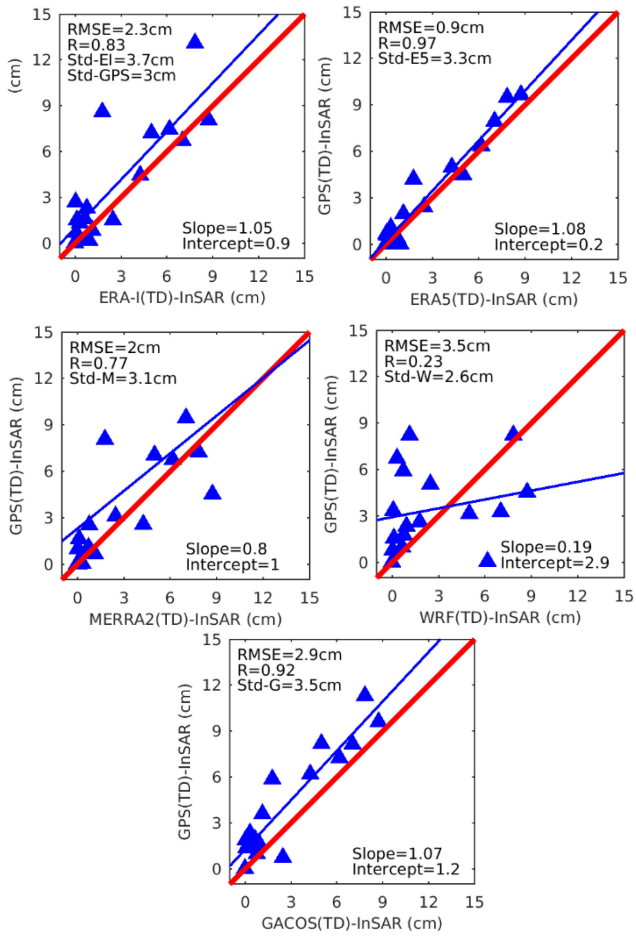

Fig. 4. Total InSAR Delay (TD-InSAR) versus GPS (TD-InSAR) for ERA-Interim, ERA5, MERRA2, WRF, and GACOS (the blue triangles). The TD-InSAR value of WRF model in the IFG no. 17 appeared as an outlier due to the poor quality of the WRF model (see the discussion section and Fig. 14). The parameters in the images are the same like in the Fig. 3, except those calculated here for InSAR delay.

D. Phase-Based Model (Nonlinear)

In the power law model, the power law decay (α) and reference height (h_0) parameters were calculated from the sounding data using (5) and (6) to estimate the interferometric phase delay (see Fig. 8).

In the spatial band selection step, a band of 8–9 km was selected as its correction presented the smallest rmse and mean rmse (i.e., 2 rad equals to 0.8 cm) compared to the ERA5 phase delay to avoid contaminating tropospheric signal with the deformation signal (the landslide extent of 1.5 $\times$ 3 km) (see Fig. 9). The ERA5 was used here as the reference due to its high accuracy derived among other NWM models. After applying the 9th band (i.e., 8–9 km), the tropospheric InSAR phase delay was estimated (see Fig. 10).

The estimated InSAR tropospheric delay maps obtained by power law do not show a good agreement with the other models. This means that the weather parameters used from sounding data do not reflect the real atmospheric conditions over the case study. The reason is probably be related to the distance

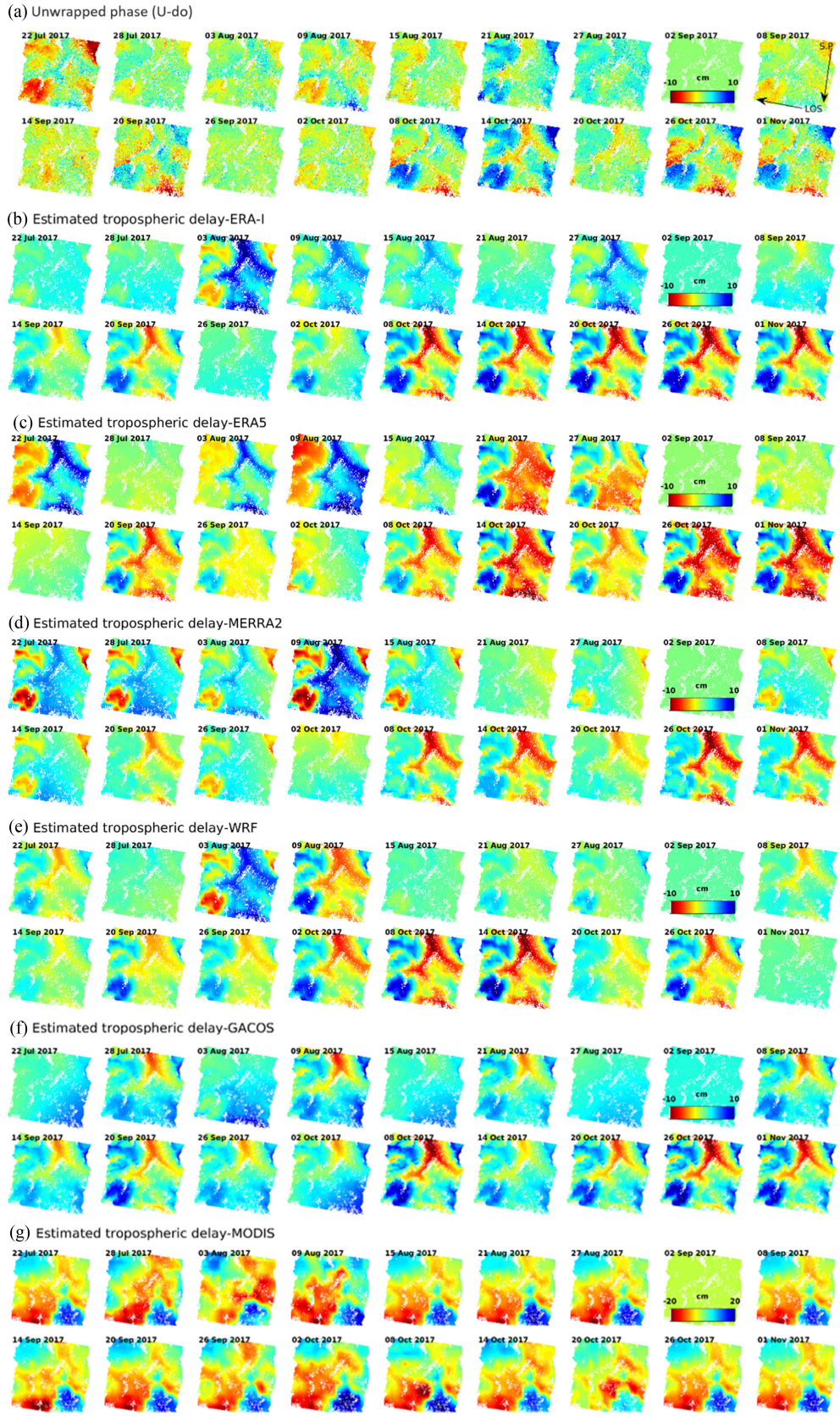

Fig. 5. Interferometric phase delays of the NWM models and MODIS. The total InSAR tropospheric delays ($T = H+W$) corresponding to each IFG of Sentinel-1 data after the DEM and orbital ramp removal (U-do) are shown. The delays derived by MODIS only show the wet component (nonfree cloud). The master data (8th IFG) has no delay (zero). LOS and satellite pass (S.P) of Sentinel-1 over the case study are shown in Fig.(a). A same color bar was set for all cases to facilitate the comparison, except for the MODIS, where the color bar limits went beyond the limits of the others cases.

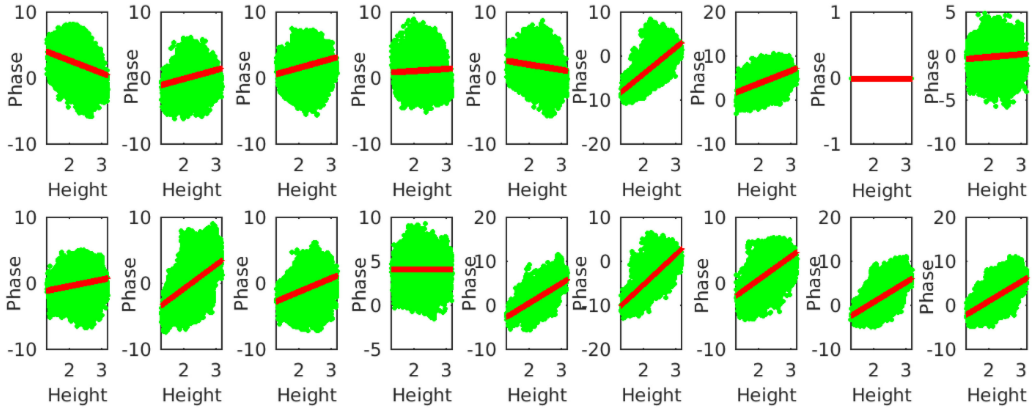

Fig. 6. Linear relation between phase and topography. The relation between height (km) and phase (cm) (green dots), and height and correlated delay estimated from the linear relationship (red line) depicted for each IFG. The 8th graph in the first row indicates the master data.

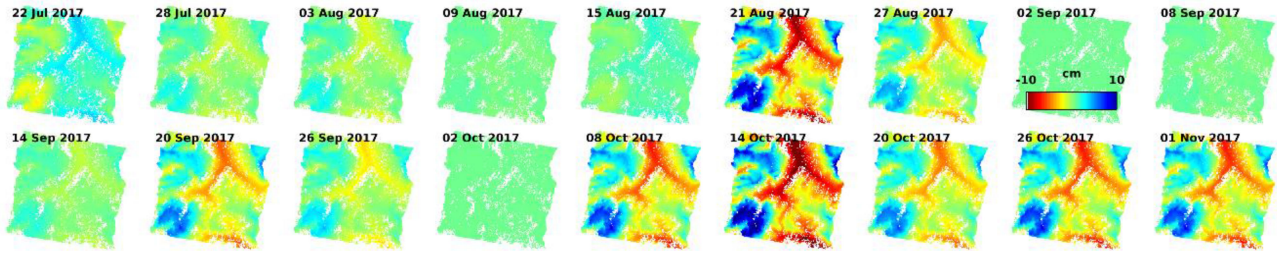

Fig. 7. Interferometric tropospheric delay estimated based on the linear relation between phase and topography.

between balloon-sounding station and our case study (nearly 100 km apart). Hence, the power low parameters (i.e., α and h_0) have been updated by estimating the refractivity using the ERA5 model instead.

In order to assess the performance of the models used in InSAR tropospheric correction, we generated the velocity maps of the study area before and after tropospheric correction of the entire scene of the local area (i.e., the landslide extent) (see Figs. 11 and 12). According to the velocity maps, some areas especially the residential region (which could considered at approximately zero velocity) in the valley [the blue λ-like-shape region in Fig. 1(b)] are completely contaminated by tropospheric artifacts ("V" and "V-do" in Fig. 11). After the tropospheric correction, the velocity values in the aforementioned valley appeared as green color referring to zero displacement. The red and blue colors surrounding the landslide are related to the mountainsides or hillsides. During the summer time, the glaciers and snow started melting and this triggered some deformations and changes that resulted in displacement on our velocity maps. As the snow melted during the summer season, the mountainsides or hillsides were highly prone to geological changes as well as water-laden masses of soil and fragmented rocks rushed down mountainsides.

The velocity maps can be visually categorized into three groups in terms of the patterns similarity: 1) ERA-Interim, ERA5, and MERRA2, 2) WRF, GACOS, and Linear, and 3) power law. To quantify the performance of each model in presence of the known deforming values (determined by the GPS measurements) the velocity map of the Corvara landslide before and after tropospheric correction was investigated. To this end, a magnified view of the velocity map of the Corvara landslide is provided in Fig. 12.

To assess the performance of each model the velocities of two GPS stations (i.e., no. 8 and 54) were compared with the corresponding points in the velocity map of the landslide after tropospheric correction within the same time span (see Fig. 12).

The main movement direction of the landslide derived by GPS observations in Fig. 1(d) can be compared with the movement direction obtained by InSAR in the velocity maps. For instance, the left part of landslide leading to the urban area that must have a near zero velocity (green color) can be used as a visual indicator to evaluate the models performance. In this respect, ERA5, MERRA2, and ERA-Interim indicate the highest agreement with a near zero velocity corresponding the urban area. Since, the movement direction of GPS no. 58 is aligned to North-to-South (which is not detectable by the SAR imaging systems), this GPS station was excluded from our validation procedure. The velocity map corrected by the power law ("V-P1") presents a relative high disagreement with respect to the other models. Thereby, its parameters were updated using the ERA5 model in (5) and the velocity map recreated ("V-P2"). A significant improvement was obtained especially in the left part of the velocity map. The quantitative values for GPS velocity and the corresponding values in the velocity maps for all the tropospheric correction models are presented in the Table II.

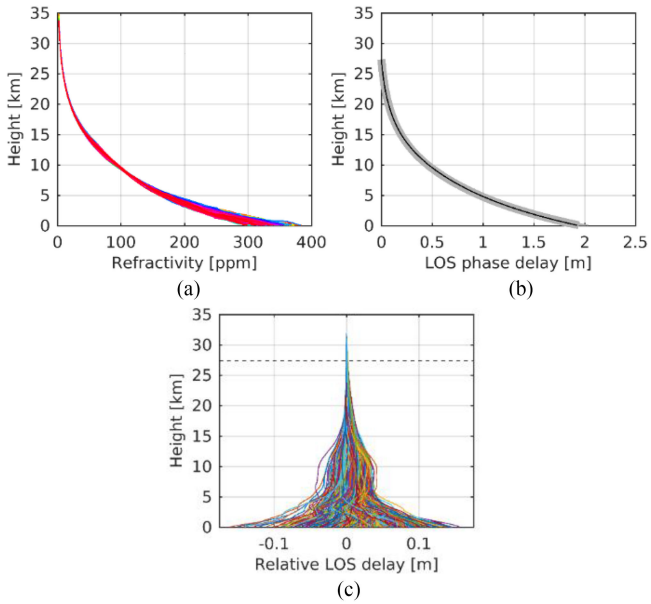

Fig. 8. Tropospheric-related phase delay parameters computed by the balloon-sounding data for 18 days (00-12 UTC) from January 22 to November 1. (a) Refractivity (wet) component calculated based on (1). (b) LOS phase delay obtained by integrating refractivity (wet+dry) over the LOS signal path up to height of 27.2 km that the phase delay reaches to zero (the solid line refers to mean delay). (c) Relative LOS phase delay presents 400 combinations of the difference among tropospheric delays at two different days to estimate h_0 (dash line). All relative LOS delay converged to zero at height $h_0 = 27.2$ km in which the standard deviations of relative delay are less than 0.05 cm. There is no relative delay between acquisitions above the dash-line (i.e., at 27.2 km).

TABLE II
UNITS FOR MAGNETIC PROPERTIES VELOCITY CROSS VALIDATION USING GPS STATIONS AS REFERENCES POINTS

GPS&Models	GPS 8	%Error 8	GPS 54	%Error 54
V_GPS	-155	-	-53	-
Vel	-113	27	-4	92.4
V_EI	-144	7	-36	32
V_E5	-148	4.5	-41	22.6
V_M	-145	6.4	-38	28.3
V_W	-138	10.9	-31	41.5
V_G	-143	7.7	-35	33.9
V_L	-143	7.7	-35	33.9
V_Pl 1	-133	14.1	-23	56.6
V_Pl 2	-135	12.9	-33	47.1

LOS velocity derived by GPS (V_GPS), velocity before tropospheric correction (Vel) and velocity after tropospheric correction with the phase and NWM -based models (V_Models) corresponding to the GPS stations no. 8 and 54 are provided. The absolute percent error was calculated for all cases. The values were rounded and the unit is in millimeter per year (mm/yr).

The error values in the Table II show that ERA5 has the lowest error among all models for both GPS stations. The errors values for GPS no. 8 are generally smaller than for GPS no. 54 for all models. This is most probably due to a velocity underestimation caused in the non-LOS motion region corresponding to the GPS station no. 54 [see Fig. 1(d)].

VI. DISCUSSION

Although the NWM data generally suffer from a coarse spatial and temporal resolution, a relative good agreement exists among GPS-derived ZTD, ZWD, and ZHD and their counterparts obtained by NWM models (see Fig. 3). In the case of ZTD parameter, GACOS and ERA5 exhibited the highest accuracy and precision among other NWMs. The GACOS yielded better accuracy (rmse = 0.8 cm) than ERA5 (rmse = 1 cm), but ERA5 provided better precision and higher correlation (std = 2.7 cm and R = 0.97) than GACOS (std = 2.8 cm and R = 0.95). To have a proper judgment about the GACOS and ERA5 performance, it is required that those have been computed with the same processing parameters. The most important parameter is the reference height (i.e., h) in (2), because the refractivity is computed up to that elevation. We set the reference height of 30 km in refractivity processing, but we do not know what reference height has been used in GACOS product. In the case of HTD and WTD parameters, ERA5, ERA-Interim, MERRA2, and WRF provided the highest accuracy, precision, and correlation, respectively (see Fig. 2).

In the estimation of total InSAR phase delay, which refers to temporal changes of refractivity rather than total refractivity (see Fig. 3), ERA5 with an accuracy and correlation of 0.9 and 0.97 cm, respectively, and MERRA2 with a precision of 3.1 cm provided the best performance among other NWM models in comparison with GPS measurements (see Fig. 4).

In order to discover the cause of the different results in ZTD and InSAR-TD estimations among NWM models (which could be potentially attributed to quality and spatio-temporal of the NWM models), the data quality investigation procedure should be performed for all NWM models. To this end, the weather parameters of the NWM models, which were used to estimate the refractivity, should be individually investigated. Temperature (which is the common variable in both hydrostatic and wet components of refractivity) and water vapor as a function of temperature and relative humidity were assessed and compared using (1).

For instance, Fig. 13 shows temperature and water vapor of ERA5 model obtained for the lower and upper part of the atmosphere. The lower atmosphere refers to the first pressure level (equal to the height of 205 m) and the upper atmosphere indicates the 37th-pressure level (equal to the height of 40 700 m). For the temperature parameter, at the upper atmosphere a regular smooth and homogeneous changes from –21° to –9° can be observed [see Fig. 13(a)], while an irregular sudden and heterogeneous changes from 6° to 35° can be seen at the lower atmosphere [see Fig. 13(b)]. The water vapor presented the same temperature-like pattern for the lower and upper atmosphere [see Fig. 13(c) and (d)]. The water vapor estimated using two parameters: 1) water vapor pressure (svp) and 2) relative humidity. The svp calculation is based on the svp for water [38] and svp for ice [39]. Comparison of weather parameter values shows that the most of the delays on InSAR phase mainly occurs at the lower part of troposphere, where the tropospheric dynamics is intensely and frequently variable.

Comparison of the temperature parameter values of the NWM models pointed out several significant items. The ERA-I and ERA5 exhibited a similar pattern with a difference in spatial resolution at all pressure levels while the temperature patterns of WRF and MERRA2 provided more discrepancy compared to

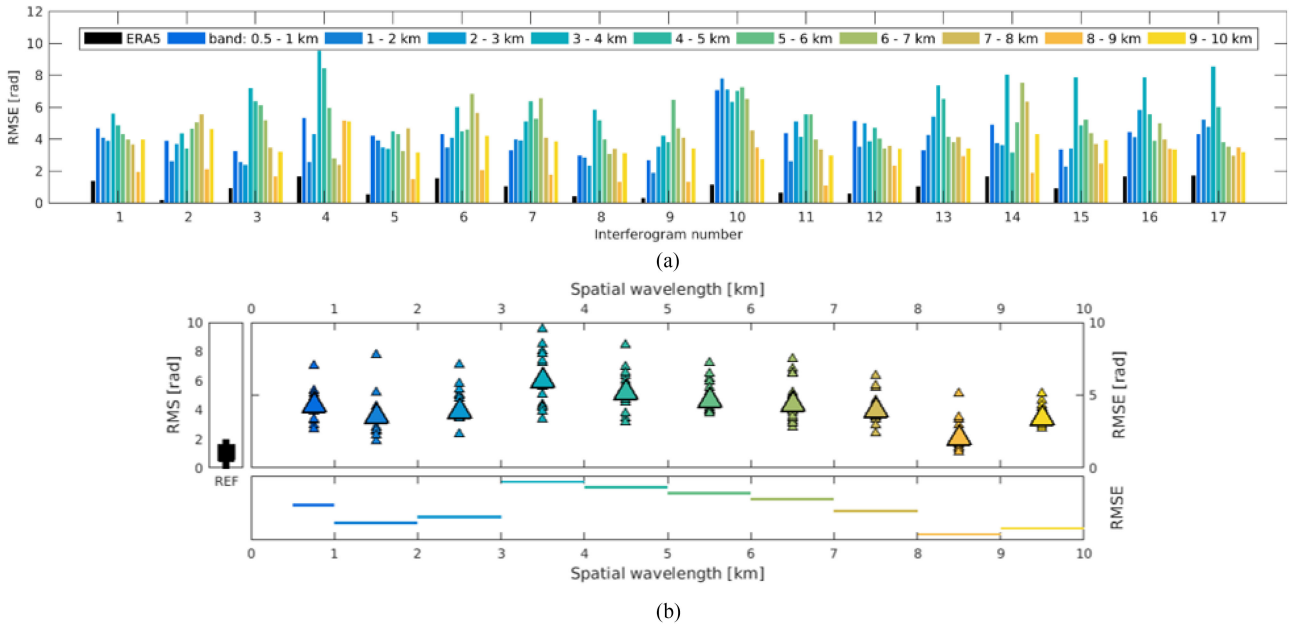

Fig. 9. Spatial band filter selection for the power law model. (a) RMSE of the different bands obtained from all IFGs and (b) mean rmse of the different spatial bands (on the bottom). The ERA5 phase delays were used to calculate the rmse as reference.

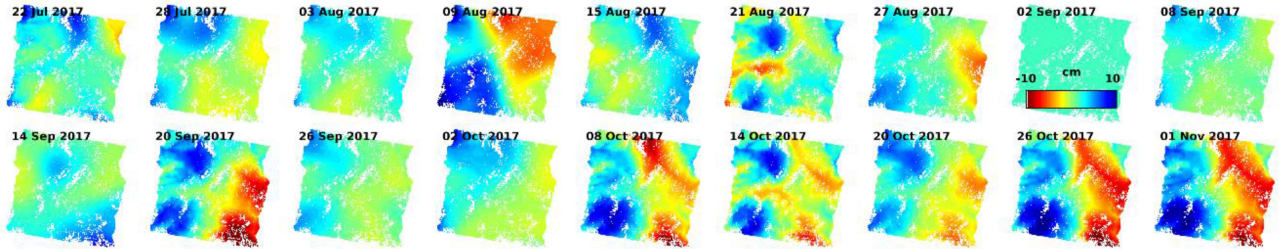

Fig. 10. Interferometric tropospheric phase delay derived by using the power law model.

ERA-I and ERA5 (see Fig. 14). ERA-I and ERA5 contained the NaN-pixels-free data, whereas WRF and MERRA2 contained the NaN pixels data at several pressure levels. The number of NaN-pixels in MERRA2 model decreases from pressure level 1 toward pressure level 10 and the pressure levels from 10 to 42 data shows lack of NaN-pixels. In WRF, the data mostly contained the NaN-pixels, especially from pressure level 1 to 10 (even in some cases completely NaN-pixels data), the pressure levels between 10 and 27 did not content NaN-pixels and at the pressure levels between 27 and 37 NaN-pixels were observed to some extent randomly (see Fig. 14).

Since interpolation was used to fill out the NaN-pixels, the interpolated pixels increased the uncertainty and impaired the refractivity estimation. This fact indicates the reason for which WRF generally provided a lower accuracy and precision results with respect to other NWM models (see Figs. 3 and 4). Departing from GPS data cross validation, we utilized two metrics as performance indicators to evaluate the models performance: 1) comparison between phase std of the original IFGs and corrected IFGs using the models (i.e., reduction rate of the IFG phase std), and 2) correlation between IFGs phase and InSAR estimated tropospheric delay. Fig. 15 depicts the phase std of all IFGs before and after phase correction and NWM-based models comprising wet, hydrostatic and total delays. The phase std reduction was then calculated for all models and IFGs (see Fig. 15).

TABLE III
PHASE STANDARD DEVIATION REDUCTION

Models	T-std red. (%)
ERA-I	77.3
ERA5	77.7
GACOS	76.2
MERRA2	76.9
WRF	77.1
Linear	80.2
Power law	72.4

Total phase standard deviation reduction (T-std red.) of 17 unwrapped IFGs derived after tropospheric correction indicated for the phase and NWM-based models.

The quantitative values of total phase std reduction for all IFGs are presented in Table III. As the Table III shows, ERA5 with 77.7% and linear with 80.2% presented the highest phase std

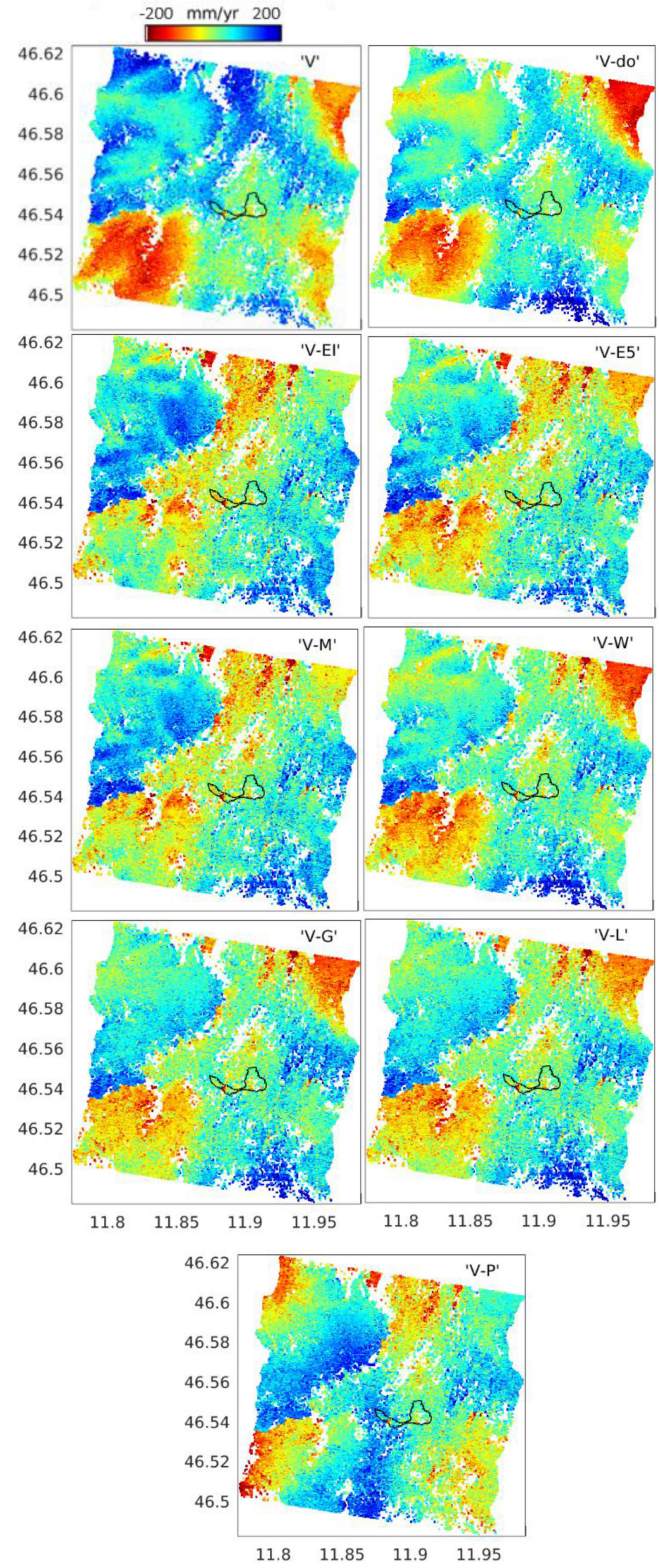

Fig. 11. Mean LOS velocity (MLV) maps. The acronyms in the plots indicate MLV without tropospheric correction ("V"), after DEM error and orbital ramp removal ("V-do"), after tropospheric correction using Entrim-I ("V-EI"), ERA5 ("V-E5"), GACOS ("V-G"), MERRA2 ("V-M"), WRF ("V-W"), power law ("V-P"), and linear ("V-L"). Negative values refers to a movement away from the satellite and positive values indicate a motion toward the satellite. The black shape in the middle of the scene indicates the Corvara landslide location.

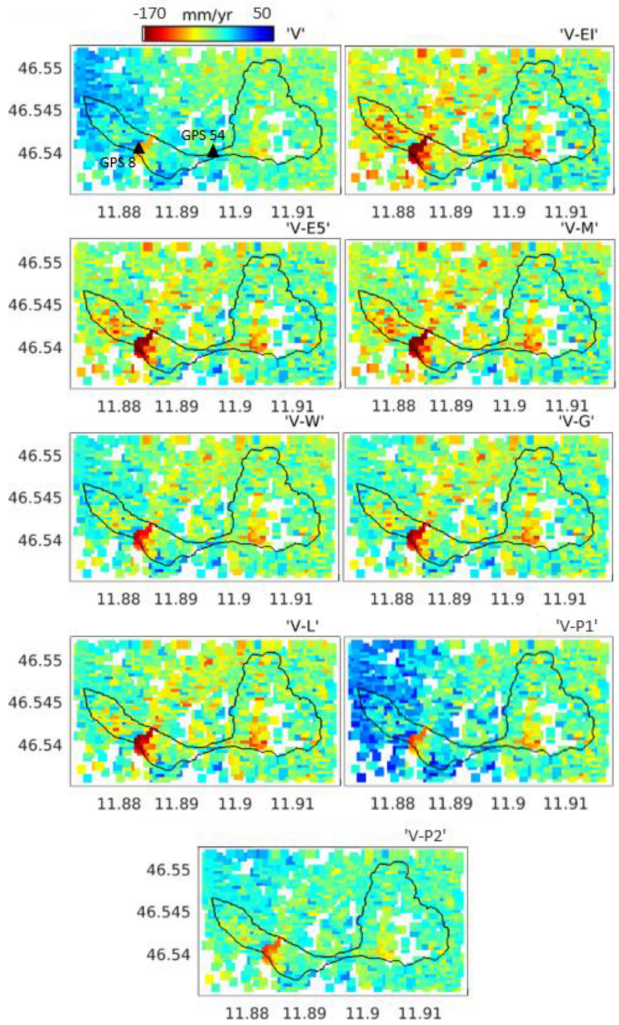

Fig. 12. Velocity maps before ("V") and after tropospheric correction ("V-Models") for Corvara landslide. Power law parameters in "V-P1" were approximated by the sounding data and their parameters were updated by the ERA5 model and the power law reestimated ("V-P2"). The black triangles present the GPS stations in the first map.

reduction for the phase and NWM-based models, respectively. The phase std reduction results generally agrees with the results of the velocity values presented in Table II except for the linear case.

The correlation (R) between IFGs phase and InSAR estimated tropospheric delay is presented in Fig. 16 as the second metrics of the performance indicator. The correlation values demonstrate how successful each intended model was in capturing tropospheric changes. MERRA2 with correlation of 0.88 and ERA5 with correlation of 0.86 provided the highest correlation coefficients among other models, corresponding to 76.9% and 77.7% in terms of phase std reduction, respectively. Considering the indicator, linear model did not present a high correction, whereas for the first indicator it provides the maximum phase std reduction. This fact implies that a single performance indicator is not able to reflect fully the performance of a model in tropospheric corrections. Therefore, the performance of models should be evaluated through several indicator metrics simultaneously.

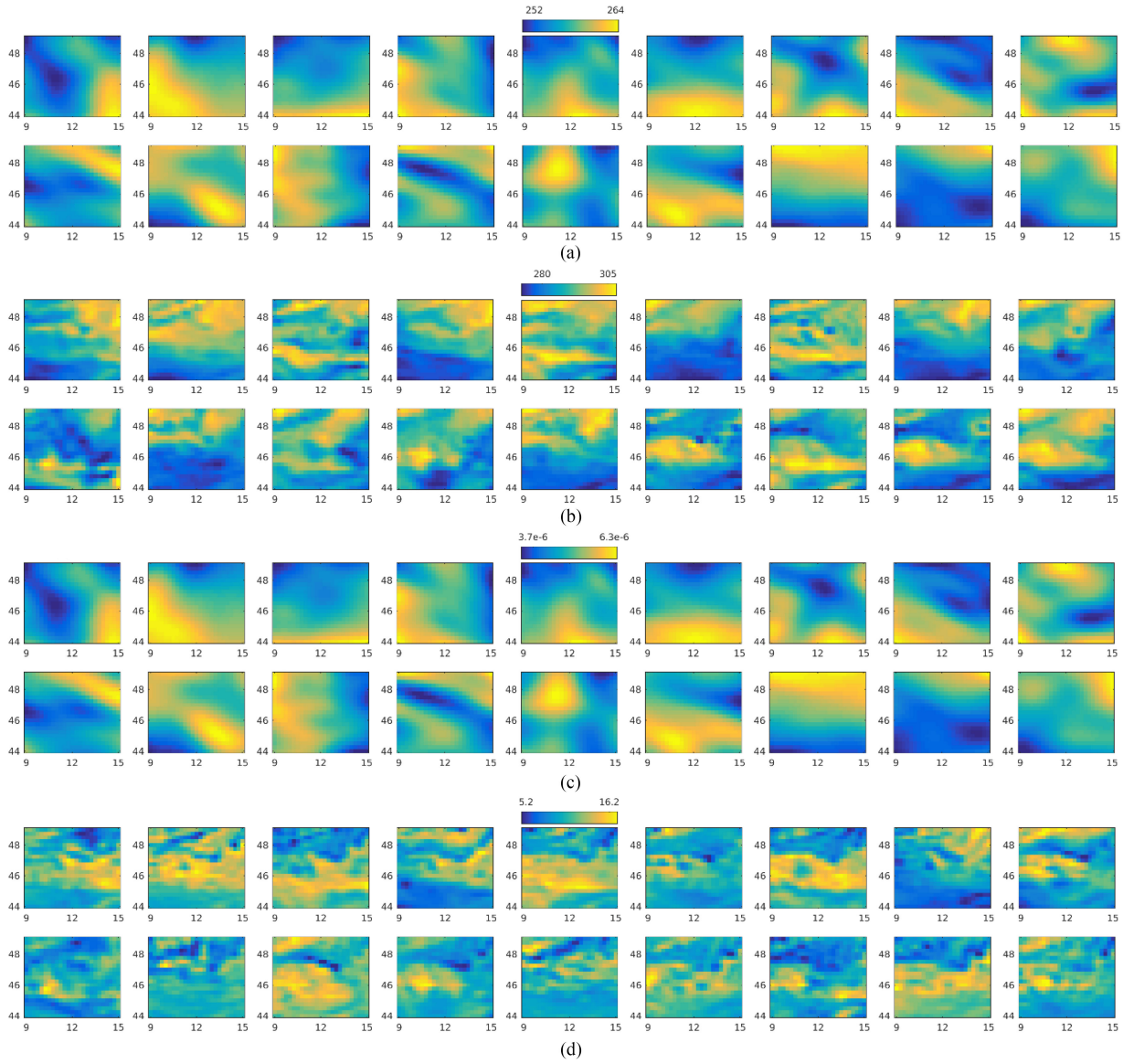

Fig. 13. Temperature (T) and water vapor (WV) of the ERA5 model. The T and WV parameters corresponding to the extent of each IFG presented for the lower and upper atmosphere.

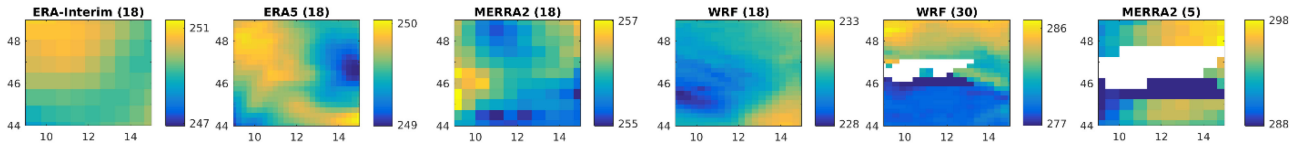

Fig. 14. Data quality check of the NWM models. Temperature parameter is shown for four NWM models at 18th pressure level (7300 m), WRF at 30th pressure level (23 000 m) and MERRA2 at 30th pressure level (1000 m). The white regions in WRF and MERRA2 data are shown the NaN-pixels.

Generally, the cross-validation results (see Fig. 2) and two indicator metrics show that ERA5 relatively outperformed other models. ERA5 has the highest temporal resolution among all the NWM models (i.e., hourly), but its spatial resolution ranks in the third place after WRF and HRES-ECMWF (GACOS) (as shown in Table I). As a result, the higher performance of ERA5 implies that the role of temporal variation in tropospheric constituent has more effect on PDE than the spatial resolution. As a NWM model with a low temporal resolution has to be interpolated (due to the difference in acquisition time between NWM model and SAR data), hence, this leads to increase uncertainty. EAR5 with the hourly resolution could effectively reduce the uncertainty and increase the accuracy and precision of PDE.

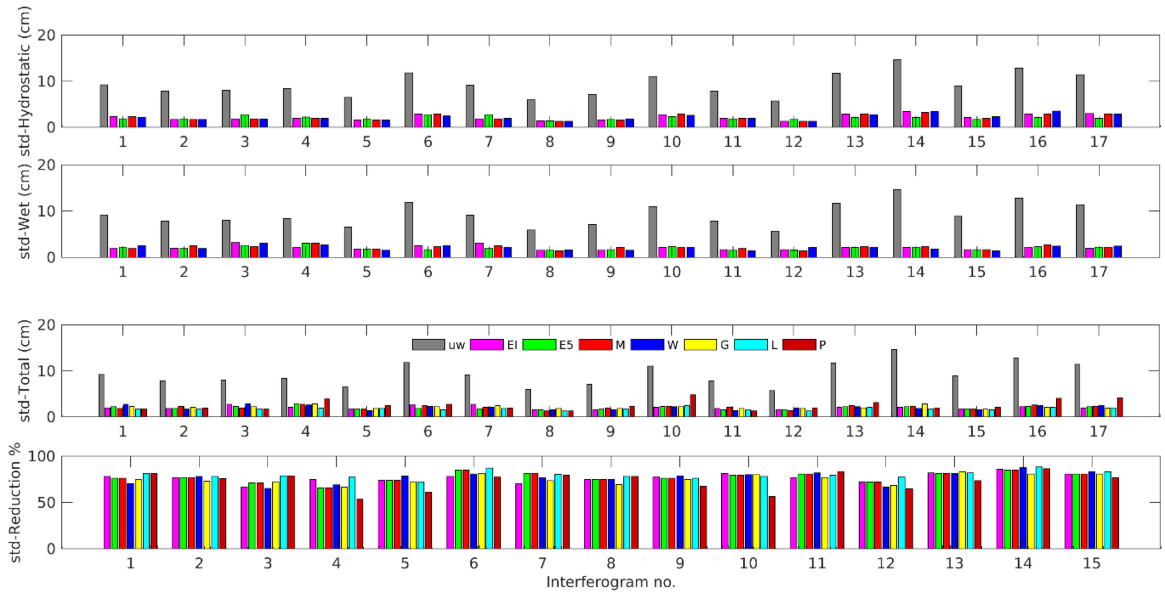

Fig. 15. Phase standard deviation reduction of wet, hydrostatic and total components after InSAR tropospheric correction for 17 IFGs. In the legend, UW indicates the unwrapped IFGs and the rest refers to the models used in tropospheric correction.

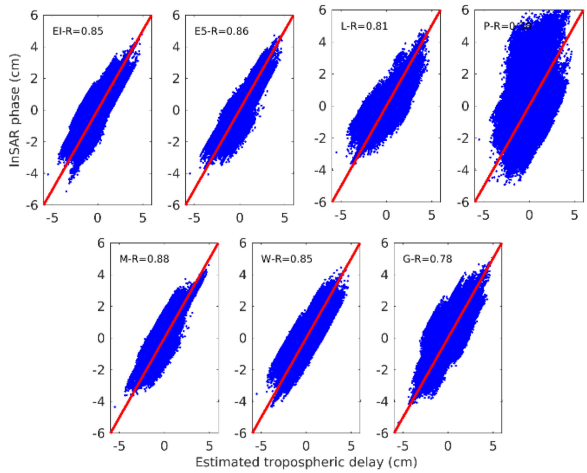

Fig. 16. Estimated tropospheric delay versus InSAR phase (unwrapped IFG). The red line is the 1:1 line.

VII. Conclusion

In this article, we investigated the performance of two main common models in InSAR and ZTD tropospheric correction contain phase-based (i.e., linear and power law) and NWM-based (Era-Interim, ERA5, MERA2 and WRF) models. We used GACOS product and GPS data as references to validate the results. The GPS-ZTD cross validation showed that ERA5 and GACOS have the highest precision (std = 2.7 cm) and accuracy (rmse = 0.8 cm) among other NWM models, respectively. The GPS-InSAR cross validation pointed out that ERA5 and MERRA2 have the highest accuracy (std = 0.9 cm) and precision (rmse = 3.1 cm), respectively. In addition to that, two indicators metrics, phase std reduction and correlation between phase and InSAR estimated tropospheric delay, were used to determine the performance and robustness of each model. Both indicators confirmed that ERA5 generally and relatively outperformed other models. The high temporal resolution of ERA5 (hourly) seems the main reason for this good performance. The data quality check procedure demonstrated that NaN-pixels in MERRA2 and WRF models induced a large bias in tropospheric refractivity estimation, especially in the WRF model. In the phase-based models part, the linear model presented a higher performance than power law (nonlinear model) in both indicators. Although re-estimation of power law parameters using ERA5 data improved the power law's performance, the proper spatial band selection is still a main challenge. In summary, the results illustrate that no single model and indicator metrics are able to fully estimate the phase delay and evaluate the performance model properly. Therefore, a combination of different data/models and the use of a set of indicator metrics should be considered simultaneously.

Acknowledgment

The authors would like to acknowledge the kind support of our research activities by the municipality of Corvara, the Ski Carosello Corvara, and the Office for Geological Surveys and Building Material Test and the Geodesy Office of the Autonomous Province of Bolzano and also would like to thanks N. D. Sclafani from Bolzano province [South Tyrolean POsitioning (STPOS)] for providing the raw GPS stations data of the Bolzano and C. Kofler for the GPS data processing of the GPS stations no. 8, 54, and 58. M. Darvishi benefits from a Ph.D. fellowship from the Autonomous Province of Bolzano under the Ext-Sat project (No. 7/06 from 12 July 2006) and the fund from ALPSMOTION (ALPine Slow slope Movement moniTorIng and detectiON with remote and proximal sensing) project. Sentinel-1 data were provided by the European Space Agency.

REFERENCES

[1] H. Fattahi, M. Simons, and P. Agram, "InSAR time-series estimation of the ionospheric phase delay: An extension of the split range-spectrum technique," *IEEE Trans. Geosci. Remote Sens.*, vol. 55, no. 10, pp. 5984–5996, Oct. 2017.

[2] H. Zebker, P. Rosen, and S. Hensley, "Atmospheric effects in interferometric synthetic aperture radar surface deformation and topographic maps," *J. Geophys.*, vol. 102, pp. 7547–7563, 1997.

[3] A. Hooper *et al.*, "Importance of horizontal seafloor motion on tsunami height for the 2011 Mw = 9.0 Tohoku-Oki earthquake," *Earth Planet. Sci. Lett.*, vol. 361, pp. 469–479, 2013.

[4] D. P. S. Bekaert, A. Hooper, and T. J. Wright, "Reassessing the 2006 Guerrero slow-slip event, Mexico," *J. Geophys. Res. B Solid Earth*, vol. 120, pp. 1357–1375, 2015.

[5] R. F. Hanssen, *Radar Interferometry: Data Interpretation and Error Analysis*, vol. 2. New York, NY, USA: Springer Science & Business Media, 2001.

[6] G. Gomba, A. Parizzi, F. De Zan, M. Eineder, and R. Bamler, "Toward operational compensation of ionospheric effects in SAR interferograms: The split-spectrum method," *IEEE Trans. Geosci. Remote Sens.*, vol. 54, no. 3, pp. 1446–1461, Mar. 2016.

[7] A. Ferretti, C. Prati, F. Rocca, and I. Politecnico, "Permanent scatterers in SAR interferometry," *Geosci. Remote Sens., IEEE Trans.*, vol. 39, no. 1, pp. 1528–1530, 1999.

[8] P. Berardino, G. Fornaro, R. Lanari, and E. Sansosti, "A new algorithm for surface deformation monitoring based on small baseline differential SAR interferograms," *IEEE Trans. Geosci. Remote Sens.*, vol. 40, no. 11, pp. 2375–2383, Nov. 2002.

[9] A. Hooper, P. Segall, and H. Zebker, "Persistent scatterer interferometric synthetic aperture radar for crustal deformation analysis, with application to Volcán Alcedo, Galápagos," *J. Geophys. Res. Solid Earth*, vol. 112, no. 7, pp. 1–21, 2007.

[10] M. P. Doin, C. Lasserre, G. Peltzer, O. Cavalié, and C. Doubre, "Corrections of stratified tropospheric delays in SAR interferometry: Validation with global atmospheric models," *J. Appl. Geophys.*, vol. 69, no. 1, pp. 35–50, 2009.

[11] F. Beauducel, P. Briole, and J.-L. Froger, "Volcano-wide fringes in ERS synthetic aperture radar interferograms of Etna (1992-1998): Deformation or tropospheric effect?" *J. Geophys. Res. Solid Earth*, vol. 105, no. B7, pp. 16391–16402, 2000.

[12] C. W. Wicks, D. Dzurisin, S. Ingebritsen, W. Thatcher, Z. Lu, and J. Iverson, "Magmatic activity beneath the quiescent three sisters volcanic center, central oregon cascade range, USA," *Geophys. Res. Lett.*, vol. 29, no. 7, pp. 2–5, 2002.

[13] D. P. S. Bekaert, A. Hooper, and T. J. Wright, "A spatially variable power law tropospheric correction technique for InSAR data," *J. Geophys. Res. Solid Earth*, vol. 120, no. 2, pp. 1345–1356, 2015.

[14] R. Jolivet, R. Grandin, C. Lasserre, M. P. Doin, and G. Peltzer, "Systematic InSAR tropospheric phase delay corrections from global meteorological reanalysis data," *Geophys. Res. Lett.*, vol. 38, no. 17, pp. 1–6, 2011.

[15] R. Jolivet *et al.*, "Improving InSAR geodesy using global atmospheric models," *J. Geophys. Res. Solid Earth*, vol. 119, no. 3, pp. 2324–2341, 2014.

[16] C. Yu, Z. Li, and N. T. Penna, "Interferometric synthetic aperture radar atmospheric correction using a GPS-based iterative tropospheric decomposition model," *Remote Sens. Environ.*, vol. 204, pp. 109–121, 2018.

[17] D. P. S. Bekaert, R. J. Walters, T. J. Wright, A. J. Hooper, and D. J. Parker, "Statistical comparison of InSAR tropospheric correction techniques," *Remote Sens. Environ.*, vol. 170, pp. 40–47, 2015.

[18] J. Jung, D. J. Kim, and S. E. Park, "Correction of atmospheric phase screen in time series InSAR using WRF model for monitoring volcanic activities," *IEEE Trans. Geosci. Remote Sens.*, vol. 52, no. 5, pp. 2678–2689, May 2014.

[19] Z. Li, E. J. Fielding, P. Cross, and R. Preusker, "Advanced InSAR atmospheric correction: MERIS/MODIS combination and stacked water vapour models," *Int. J. Remote Sens.*, vol. 30, no. 13, pp. 3343–3363.

[20] Z. W. Li *et al.*, "Correcting atmospheric effects on InSAR with MERIS water vapour data and elevation-dependent interpolation model," *Geophys. J. Int.*, vol. 189, no. 2, pp. 898–910, 2012.

[21] S. Williams, Y. Bock, P. Fang, and H. Cecil, "Aperture radar products," *Network*, no. 98, pp. 51–67, 1998.

[22] P. W. Webley, R. M. Bingley, A. H. Dodson, G. Wadge, S. J. Waugh, and I. N. James, "Atmospheric water vapour correction to InSAR surface motion measurements on mountains: Results from a dense GPS network on Mount Etna," *Phys. Chem. Earth*, vol. 27, no. 4–5, pp. 363–370, 2002.

[23] F. Onn and H. A. Zebker, "Correction for interferometric synthetic aperture radar atmospheric phase artifacts using time series of zenith wet delay observations from a GPS network," *J. Geophys. Res. Solid Earth*, vol. 111, no. 9, pp. 1–16, 2006.

[24] Z. Li, J.-P. Muller, P. Cross, and E. J. Fielding, "Interferometric synthetic aperture radar (InSAR) atmospheric correction: GPS, moderate resolution imaging spectroradiometer (MODIS), and InSAR integration," *J. Geophys. Res. Solid Earth*, vol. 110, no. B3, p. 2, 2005.

[25] Y. N. N. Lin, M. Simons, E. A. Hetland, P. Muse, and C. Dicaprio, "A multiscale approach to estimating topographically correlated propagation delays in radar interferograms," *Geochem., Geophys. Geosyst.*, vol. 11, no. 9, pp. 1–17, 2010.

[26] J. R. Elliott, J. Biggs, B. Parsons, and T. J. Wright, "InSAR slip rate determination on the Altyn Tagh Fault, northern Tibet, in the presence of topographically correlated atmospheric delays," *Geophys. Res. Lett.*, vol. 35, no. 12, pp. 1–5, 2008.

[27] E. K. Smith and S. Weintraub, "The constants in the equation for atmospheric refractive index at radio frequencies," *Proc. IRE*, vol. 41, no. 8, pp. 1035–1037, 1953.

[28] B.-C. Gao and Y. J. Kaufman, "Water vapor retrievals using moderate resolution imaging spectroradiometer (MODIS) near-infrared channels," *J. Geophys. Res. Atmos.*, vol. 108, no. D13, p. 4, 2003.

[29] Z. Li, J.-P. Muller, and P. Cross, "Comparison of precipitable water vapor derived from radiosonde, GPS, and moderate-resolution imaging spectroradiometer measurements," *J. Geophys. Res. Atmos.*, vol. 108, no. D20, p. 10, 2003.

[30] A. Corsini, A. Pasuto, and M. Soldati, "Geomorphological investigation and management of the corvara landslide (Dolomites, Italy)," *JGU Trans.*, vol. 20, no. 3, pp. 169–186, 1999.

[31] R. Schlögel, B. Thiebes, I. Toschi, T. Zieher, M. Darvishi, and C. Kofler, "Sensor data integration for landslide monitoring—the LEMONADE concept," in *Advancing Culture of Living With Landslides: Volume 2 Advances in Landslide Science*, M. Mikos, B. Tiwari, Y. Yin, and K. Sassa, Eds. Cham, Switzerland: Springer International Publishing, 2017, pp. 71–78.

[32] M. Darvishi, R. Schlögel, L. Bruzzone, and G. Cuozzo, "Integration of PSI, MAI, and intensity-based sub-pixel offset tracking results for landslide monitoring with X-band corner reflectors-Italian Alps (Corvara)," *Remote Sens.*, vol. 10, no. 3, 2018.

[33] M. Darvishi *et al.*, "Sentinel-1 and ground-based sensors for continuous monitoring of the Corvara landslide (South Tyrol, Italy)," *Remote Sens.*, vol. 10, no. 11, 2018, Art. no. 1781.

[34] A. Hooper, H. Zebker, P. Segall, and B. Kampes, "A new method for measuring deformation on volcanoes and other natural terrains using InSAR persistent scatterers," *Geophys. Res. Lett.*, vol. 31, no. 23, pp. 1–5, 2004.

[35] W. Shamarock *et al.*, "A description of the advanced research WRF version 3," Tech. Rep., NCAR/TN-475+STR, University Corporation for Atmospheric Research, Boulder, CO, USA, 2008.

[36] T. Herring, R. W. King, M. A. Floyd, and S. C. McClusky, "GAMIT reference manual. GPS analysis at MIT GLOBK, release 10.6," no. p. 168, 2015.

[37] J. Boehm, B. Werl, and H. Schuh, "Troposphere mapping functions for GPS and very long baseline interferometry from European Centre for medium-range weather forecasts operational analysis data," *J. Geophys. Res. Solid Earth*, vol. 111, no. 2, pp. 1–9, 2006.

[38] A. L. Buck, "New equations for computing vapor pressure and enhancement factor," *J. Appl. Meteorol.*, vol. 20, no. 12, pp. 1527–1532, 1981.

[39] O. A. Alduchov and R. E. Eskridge, "Improved Magnus form approximation of saturation vapor pressure," *J. Appl. Meteorol.*, vol. 35, no. 4, pp. 601–609, 1996.

Mehdi Darvishi received the B.Sc. and M.Sc. degrees in telecommunication engineering and remote sensing from the Department of Information Engineering and Computer Science, University of Trento, Trento, Italy. He is currently working toward the Ph.D. degree in information and telecommunication technologies with the Department of Information Engineering and Computer Science, University of Trento, Trento, Italy.

His research interests include application of remote sensing and InSAR in natural hazards monitoring.

Giovanni Cuozzo (Member, IEEE) received the M.Sc. degree in telecommunication engineering from the University Federico II of Naples, Naples, Italy in 2003 and the Ph.D. degree in electric engineering and information technology from the University of Cassino, Cassino, Italy, in 2006.

Since 2010, he has been with the EURAC-Institute of Earth Observation department, Bolzano, Italy as a Senior Researcher. His research interests include InSAR, soil moisture estimation using SAR data, statistical signal modeling and segmentation and compression of optical and SAR data.

Lorenzo Bruzzone (Fellow, IEEE) received the M.S. (*Laurea*) degree *(summa cum laude)* in electronic engineering and the Ph.D. degree in telecommunications from the University of Genoa, Genoa, Italy, in 1993 and 1998, respectively.

He is currently a Full Professor of telecommunications with the University of Trento, Trento, Italy, where he teaches remote sensing, radar, and digital communications. He is also the Founder and the Director of the Remote Sensing Laboratory, Department of Information Engineering and Computer Science, University of Trento, Trento, Italy. He is a Principal Investigator of many research projects. Among others, he is also a Principal Investigator of the Radar for Icy Moon Exploration instrument in the framework of the JUpiter ICy moons Explorer Mission with the European Space Agency. He has authored or coauthored 218 scientific publications in referred international journals (157 in IEEE journals), more than 290 papers in conference proceedings, and 21 book chapters. He has edited/coedited 18 books/conference proceedings and one scientific book. He promotes and supervises research on these topics within the frameworks of many national and international projects. His research interests include the areas of remote sensing, radar and synthetic aperture radar, signal processing, machine learning, and pattern recognition.

Dr. Bruzzone has been a member of the Administrative Committee of the IEEE Geoscience and Remote Sensing Society (GRSS), since 2009. He is currently a member of the Permanent Steering Committee of the IEEE International Workshop on the Analysis of Multi-Temporal Remote-Sensing Images series. He was the recipient of the First Place in the Student Prize Paper Competition at the 1998 IEEE International Geoscience and Remote Sensing Symposium (IGARSS), Seattle. He was also a recipient of many international and national honors and awards, including the IEEE GRSS 2015 Outstanding Service Award and the 2017 IEEE IGARSS Symposium Prize Paper Award. Since 2003, he has been the Chair of the Society of Photographic Instrumentation Engineers Conference on Image and Signal Processing for Remote Sensing. He has been the Founder of the *IEEE Geoscience and Remote Sensing Magazine*. He was a Guest Co-Editor of many special issues of international journals. He is the Co-Founder of the IEEE International Workshop on the Analysis of Multi-Temporal Remote-Sensing Images series. He was the Editor-in-Chief for the IEEE GEOSCIENCE AND REMOTE SENSING MAGAZINE from 2013 to 2017. He is an Associate Editor for the IEEE TRANSACTIONS ON GEOSCIENCE AND REMOTE SENSING. He was invited as a Keynote Speaker in more than 30 international conferences and workshops. He was a Distinguished Speaker of the IEEE Geoscience and Remote Sensing Society from 2012 to 2016. His papers are highly cited, as proven by the total number of citations (over 26 644) and the value of the h-index (74) (source: Google Scholar).

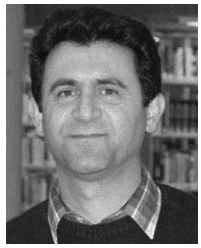

Faramarz Nilfouroushan received the B.S. degree in surveying engineering and the M.S. degree in geodesy from K. N. Toosi University, Tehran, Iran, in 1991 and 1996, respectively. He received the Ph.D. degree in geodynamics from Uppsala University, Uppsala, Sweden, in 2007.

He is currently a Geoscientist. In 2003, he was a recipient of the Ph.D. scholarship by Uppsala University. In 2008–2009, he undertook his postdoctoral research in geodynamics with the University of Toronto. In 2015, he was qualified as a Docent at Uppsala University. He is currently a Senior Lecturer in applied geodesy with the University of Gävle and is Senior Geodesist with the Swedish land survey (Lantmäteriet). He has a vast experience in tectonic geodesy, where he uses satellite geodetic data (GNSS and InSAR) for analysis of crustal deformation. Moreover, he has significant experience in tectonic simulation of fold-and-thrust belts using physical models. He has contributed to a large amount of peer-reviewed papers published in international journals (some with hundreds of citations) and also contributed to many international meetings and workshops.